Plasmon Emission Quantum Yield of Single Gold Nanorods as a Function of Aspect Ratio

Ying Fang,[†] Wei-Shun Chang,[†] Britain Willingham,[†] Pattanawit Swanglap,[†] Sergio Dominguez-Medina,[†] and Stephan Link[†,‡,*]

[†]Department of Chemistry and [‡]Department of Electrical and Computer Engineering, Laboratory for Nanophotonics, Rice University, Houston, Texas 77005, United States

ABSTRACT

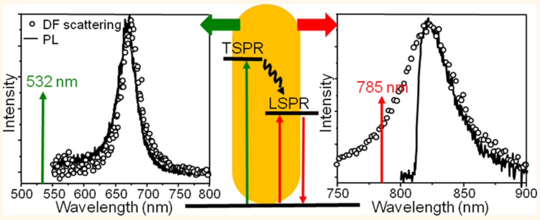

We report on the one-photon photoluminescence of gold nanorods with different aspect ratios. We measured photoluminescence and scattering spectra from 82 gold nanorods using single-particle spectroscopy. We found that the emission and scattering spectra closely resemble each other independent of the nanorod aspect ratio. We assign the photoluminescence to the radiative decay of the longitudinal surface plasmon generated after fast interconversion from excited electron–hole pairs that were initially created by 532 nm excitation. The emission intensity was converted to the quantum yield and was found to approximately exponentially decrease as the energy difference between the excitation and emission wavelength increased for gold nanorods with plasmon resonances between 600 and 800 nm. We compare this plasmon emission to its molecular analogue, fluorescence.

KEYWORDS: **photoluminescence · surface plasmons · gold nanorods · plasmon emission · electron–hole pairs**

Photoluminescence (PL), in which a photon is emitted by an atom, molecule, or nanoparticle after the absorption of another photon, has been important for many technologies. A specific type of PL, fluorescence, is widely used in modern scientific research, with applications ranging from sensing, imaging, quantitative analysis, to lighting.[1−3] Due to the inevitable limitations of fluorescence, photobleaching and photoblinking, it is of current interest to study the PL from more robust nanostructures, that is, *artificial molecules*, such as inorganic nanocrystals[4] or carbon nanotubes.[5] Among them, gold nanoparticles have attracted special attention due to their high biocompatibility and thermal robustness.[6−9] However, the detailed mechanism of the PL in gold nanoparticles still remains an open question. In most artificial molecules, an electron–hole pair, or exciton, is excited and then radiatively recombines, generating the PL. This process is typically very inefficient in metals[10] but can be enhanced by the local surface plasmon field.[11−19] In contrast, other studies on gold nanoparticles smaller than 100 nm have instead assigned the PL to the radiative decay of the surface plasmon.[20−23]

For fluorescence in most molecular systems, the energy separation between excited states is smaller than the one between the lowest excited state and the ground state. This leads to an initial fast nonradiative relaxation to the first excited state. Therefore, the fluorescence quantum yield remains constant regardless of the excitation wavelength. This is well-known as the Kasha–Vavilov rule.[24,25] With very few exceptions,[4,26] this rule holds true for most artificial molecules, but there are no studies regarding the applicability of a similar rule to the PL quantum yield of metal nanoparticles.

Gold nanorods (AuNRs) represent an excellent model system for studying energy relaxation in an artificial molecule. Unlike gold nanospheres, which only have one plasmon mode and for which the PL yield has been observed to be independent of size,[27] AuNRs have a longitudinal surface plasmon resonance (LSPR) that is easily tunable from ~600 nm to the near-infrared by increasing the AuNR aspect ratio.[28] In addition, a small, mostly size-insensitive absorption feature exists below 550 nm due to the combination of the transverse surface plasmon resonance (TSPR) and interband transitions. Because excitation of these transitions at shorter wavelengths leads mainly to emission by the LSPR,[23] it is possible to easily separate the PL from elastic scattering. Moreover, by increasing

* Address correspondence to slink@rice.edu.

Received for review May 21, 2012 and accepted July 25, 2012.

10.1021/nn3022469

the AuNR aspect ratio and thus red-shifting the LSPR, one can study an artificial molecule with a variable gap between the absorption and emission states. Instead of tuning the excitation wavelength as in the case of molecules to which the Kasha–Vavilov rule applies, we here changed the aspect ratio of single AuNRs while keeping the excitation wavelength the same in order to examine how the intrinsic PL from AuNRs scales with the energy gap between excitation and emission. We consider this experiment as a nanoparticle analogue of the Kasha–Vavilov rule because by increasing the AuNR aspect ratio the electronic energy levels are not affected except for the LSPR maximum.

RESULTS AND DISCUSSION

Single-particle imaging and spectroscopy correlated with scanning electron microscopy (SEM) were essential to exclude effects due to sample heterogeneity and impurities. Commercially available AuNRs, which we first characterized by transmission electron microscopy (TEM) and extinction spectroscopy (Figure S1 in the Supporting Information), were spin-coated at low concentrations on quartz substrates. Markers were added to the substrate for identification of the same single AuNRs in SEM and optical microscopy.[29,30] Figure 1A shows a typical PL image of individual AuNRs and a dimer. The high-magnification SEM images of the corresponding AuNRs are included in Figure 1A (see Figure S2 for the low-magnification SEM image). The PL was excited with a circularly polarized 532 nm laser and detected by an avalanche photodiode. Images were recorded by scanning the sample (see Figure S3 for a scheme of the microscope setup).

Despite the low quantum yield, the PL images were more sensitive than the dark-field (DF) scattering images on the same microscope. Figure 1B shows the corresponding DF scattering image. Comparison to the PL image shows that two of the AuNRs are not sufficiently resolved by DF scattering. The higher sensitivity for PL imaging is mainly due to a better spatial resolution because the laser could be focused to a diffraction-limited spot. In addition, the PL is not as biased toward larger nanostructures because it scales as absorption with the particle volume instead of as scattering with the volume squared.[23,27]

To determine quantum yields, we measured the PL spectra of individual AuNRs. Single AuNR spectra were collected by moving the sample to the location of a single AuNR and switching the detection to a spectrometer equipped with a CCD camera. The wavelength response of the collection system was corrected by a calibrated white light lamp (Figure S4). Figure 2A shows the normalized PL spectra of four AuNRs with different aspect ratios. The spectral shape of the PL follows closely that of surface plasmon scattering.

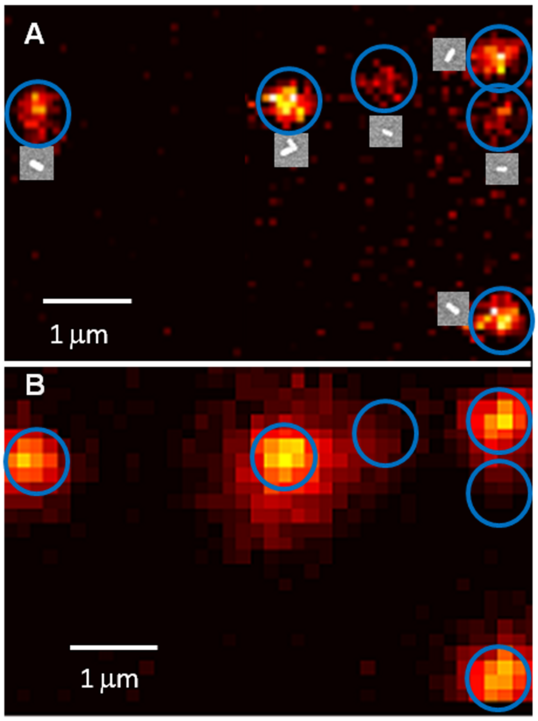

Figure 1. (A) PL image of AuNRs. (B) Corresponding DF scattering image. Correlated high-magnification SEM images are shown in A next to the PL signal.

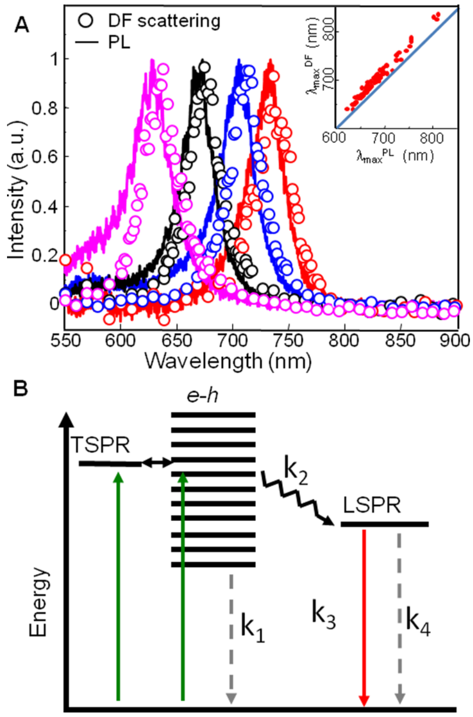

Figure 2. (A) Normalized PL (solid line) and DF scattering (open circles) spectra of single AuNRs. Inset: Relationship between the PL and DF scattering maxima, λ_{max}^{PL} and λ_{max}^{DF}. For nearly all AuNRs, $\lambda_{max}^{PL} < \lambda_{max}^{DF}$. (B) Three-step model for the PL.

Simultaneous PL and DF imaging and spectroscopy furthermore allowed us to distinguish single AuNRs from clusters and impurities based on image patterns and spectral signatures, especially in the absence of correlated SEM data. The spectra of single AuNRs showed only one band that was characteristic of the LSPR mode, while spectra of aggregates had several features because of plasmon coupling. Interestingly, the spectral response of AuNR aggregates was different between PL and DF scattering (Figure S5).

The close resemblance between the PL and DF scattering spectra independent of the aspect ratio measured for 82 single AuNRs is consistent with our previously suggested mechanism of plasmon emission.[23] Plasmon emission occurs due to radiative decay of a plasmon that has been created from an excited electron–hole pair after absorption of a 532 nm photon, as illustrated in Figure 2B. At 532 nm, both the TSPR and interband transitions are excited for the AuNRs studied. Although, due to their spectral overlap, we are not able to separate these two excitation pathways, it is known from photoelectron spectroscopy that the TSPR quickly generates electron–hole pairs.[31–33] The hot electrons lose their energy nonradiatively and then interconvert to the LSPR mode, which emits a photon. A direct interconversion between the TSPR and LSPR modes without the involvement of electron–hole pairs is not possible because of the orthogonal nature of these plasmons. In addition, results obtained with an excitation wavelength of 488 nm (Figure S6), which only excites interband transitions, also revealed a close resemblance between the PL and scattering spectra, further suggesting that electron–hole pairs are responsible for exciting the LSPR mode, which subsequently emits. The re-excitation of the LSPR by a hot electron should be possible based on reversibility arguments and considering that plasmon modes can be excited by electrons as in electron energy loss spectroscopy (EELS).[34]

The close resemblance between the PL and DF scattering spectra is, however, not a definite proof of the suggested plasmon emission mechanism. Instead, any luminescence process could radiate through the AuNR antenna, giving an optical response that follows the plasmon resonance with respect to the spectral shape as well as the polarization dependence (Figure S7 shows that the PL emission has a perfect dipole response along the long axis of the AuNR). Especially at 532 nm and shorter wavelengths, interband transitions are also excited and their radiative recombination has previously been assigned to the origin of the observed PL.[17,35] While we cannot rule out that the plasmon merely acts as a radiating dipole antenna, we can, however, exclude that interband transitions are the cause of the PL. To show this, we collected the PL spectrum of a single AuNR using 785 nm (1.58 eV) excitation, which is well below the 1.8 eV band gap around the X region for the interband transitions in gold.[11,16,18] Figure 3 compares the PL and DF scattering spectra and illustrates that again the PL resembles the DF scattering even though part of the PL spectrum was blocked by the dichroic as 785 nm excitation was resonant with the blue edge of the LSPR. The excitation power dependence was again linear, and the PL was polarized along the main AuNR axis.

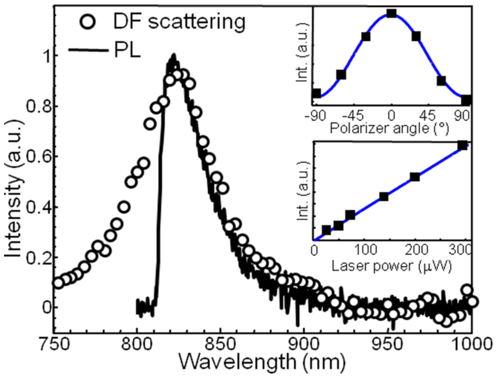

Figure 3. Single AuNR PL spectrum with 785 nm excitation and corresponding DF scattering spectrum. The AuNR was embedded in a polyvinyl alcohol matrix to red shift the LSPR. Top inset: PL intensity as a function of emission polarization, where 0° was parallel to the long AuNR axis as determined from the polarization-dependent scattering. Bottom inset: linear dependence of the PL intensity on the excitation power indicates a one-photon process.

Closer inspection of the LSPR maximum revealed that there was a small but reproducible spectral blue shift of the PL compared to the DF scattering independent of the AuNR aspect ratio. The inset in Figure 2A shows the correlation between the PL and DF scattering maxima, λ_{max}^{PL} and λ_{max}^{DF}, for 82 single AuNRs. The blue line indicates the trend if $\lambda_{max}^{PL} = \lambda_{max}^{DF}$. The value of λ_{max}^{PL} was almost universally blue-shifted by an average amount of 11 ± 3 nm. An excitation power dependence furthermore showed that λ_{max}^{PL} decreased with increasing laser power (Figure S8) and also confirmed a one-photon process (Figure S9). Laser-induced melting into smaller aspect ratio AuNRs can be excluded because the DF scattering spectra recorded before and after measuring the PL were the same (Figure S10). A thermal effect due to a change in the refractive index because of continued laser excitation is also unlikely because the temperature increase was estimated to be smaller than 10 K under our experimental conditions (see the Supporting Information for further discussion). A difference in the angular distribution of the PL and DF scattering, imaged through a high numerical aperture (NA) objective, could also lead to small differences in the spectral shape.[36,37] However, when we changed the NA from 0.8 to 0.6, we observed no significant difference (Figure S11). Another possible explanation is that the blue shift of the PL spectrum was caused by charging of the AuNRs through reactions of the environment with the hot electrons and holes as effective higher electron densities cause blue shifts of the LSPR.[38] To address this hypothesis, we collected DF scattering spectra under simultaneous 532 nm laser illumination as a function of

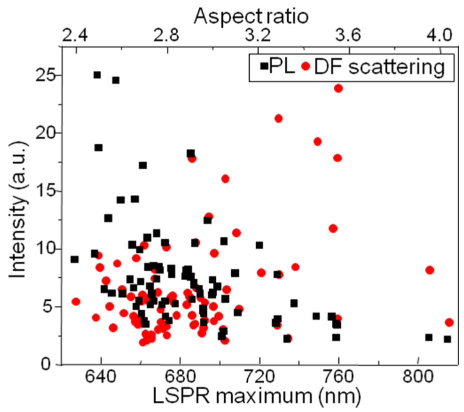

Figure 4. PL and DF scattering intensities as a function of LSPR maximum for 82 AuNRs. The LSPR maximum was converted into an aspect ratio and is included as the top *x*-axis.

laser power. While the DF scattering spectra were also blue-shifted with laser excitation (see Figure S12 for an example and Table S1 for a summary of peak shifts measured for different AuNRs and laser powers), the blue shift of the corresponding PL peak was always more pronounced. Although these results indeed suggest a dynamic, photoinduced charging process, further investigations are needed to completely resolve the underlying mechanism.

AuNRs are an ideal system to study the dependence of the quantum yield on the energy gap between absorption and emission states, considering that only the LSPR and not the TSPR or intrinsic interband transitions is shifted by an increase of the aspect ratio.[28] Therefore, the PL intensity at the LSPR region for each single AuNR was integrated. The result is shown in Figure 4 as a function of the LSPR maximum and AuNR aspect ratio (top *x*-axis), which was obtained from its linear dependence on the LSPR maximum (Figure 5).[39] The DF scattering intensities for all 82 single AuNRs are also given in Figure 4. The data presented in Figure 4 show that, in general, the PL intensity decreased with increasing AuNR aspect ratio and LSPR maxima, whereas the DF scattering intensity increased under the same conditions. As the volume of the AuNRs slightly decreased with increasing aspect ratio (based on the size distribution shown in Figure S1), the trend of the DF scattering is not as pronounced as expected. This change in PL intensity is unexpected if the limiting step was the emission instead of the internal conversion to the LSPR mode, as is the case for molecules according to the Kasha–Vavilov rule. However, to gain further insight, we need to compare quantum yields instead of PL intensities.

To calculate the quantum yield from the PL intensity, we need to account for the size-dependent absorption cross section of the AuNRs. We therefore calculated the absorption spectra for eight AuNRs of different aspect ratios at a constant width of 25 nm (Figure 5A) using

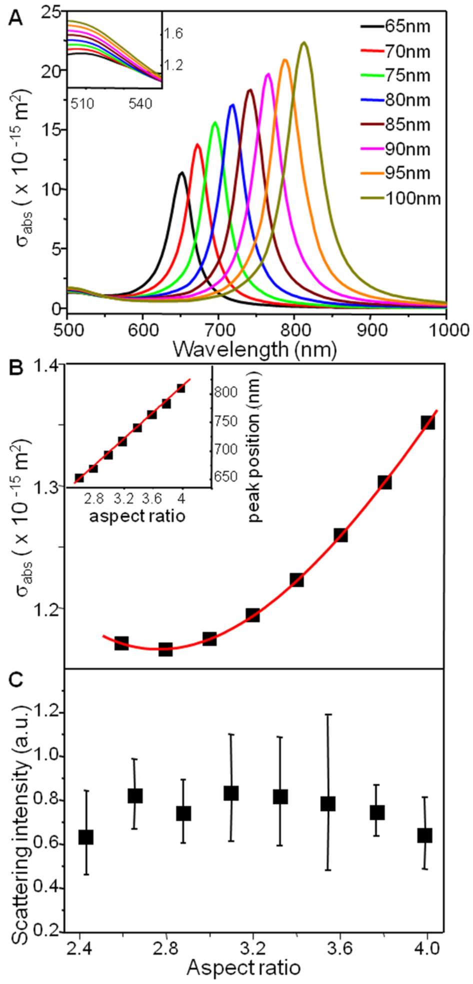

Figure 5. (A) Absorption spectra for different AuNRs with width fixed at 25 nm and lengths given by the legend. Inset: Zoom-in around the excitation wavelength of 532 nm. (B) Absorption cross section at 532 nm for the AuNRs from panel A with the red curve being a polynomial fit. Inset: Linear relationship between the LSPR maximum and the aspect ratio. (C) Aspect ratio dependence of the calculated scattering intensity. As the aspect ratio changed for the actual AuNRs in the experiment, the calculated scattering intensity was corrected using the experimental dependence of the AuNR width on the aspect ratio, as given in Figure S1B. The data show that the scattering intensity is independent of the AuNR aspect ratio.

the commercial software package COMSOL. The length was varied from 65 to 105 nm. The inset is a zoom-in for the region around 532 nm. At 532 nm, the absorption cross section is not very sensitive to the aspect ratio as it only increases by 20% when the aspect ratio is doubled (Figure 5B). The dependence of the LSPR maximum on the aspect ratio, as obtained from these calculations, is also displayed in the inset of Figure 5B. This dependence was used to convert between LSPR maxima and aspect ratios. Figure 5C shows the calculated integrated scattering intensities for the LSPR, which have been corrected by the experimental width dependence on the aspect ratio (Figure S1B). To match the data in Figure S1B to the calculations, the range of

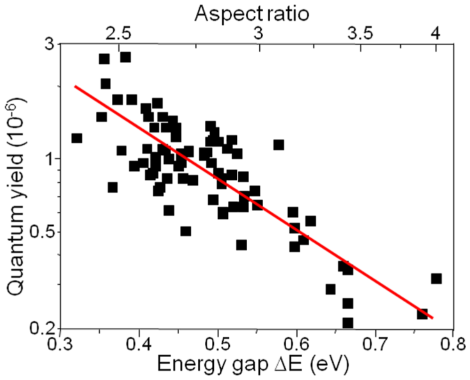

Figure 6. PL quantum yield as a function of the energy gap between absorption and emission states for 82 AuNRs. The red line is a linear fit as a guide to the eye only.

AuNR aspect ratios was first divided into eight equal parts between 2.5 and 4.1 with an interval of 0.2. The correction involved dividing the calculated scattering intensity by the sixth power of the ratio of the calculated to actual width as scattering scales with the volume squared. The data in Figure 5C show that the scattering intensity is mostly independent of the AuNR aspect ratio.[39] Thus the span of scattering intensities seen in Figure 4 is likely due to differences in the AuNR volume, consistent with our analysis.

In contrast to the weak dependence of the absorption cross section on the aspect ratio, the total absorption strongly depends on the overall size of the AuNRs as it is proportional to the volume.[27] This has a significant effect on the final quantum yield because the actual mean diameter of our AuNRs decreased from 30 to 15 nm with increasing aspect ratio (Figure S1B). Calculations for all individual AuNRs based on the dimensions obtained from high-resolution SEM are not feasible. However, this problem of correcting the quantum yield for each single AuNR can nevertheless be accomplished by considering that the DF scattering intensity scales with the square of the particle volume. We can therefore exclude the effects of volume fluctuations on the absorption cross section by dividing the measured PL intensity by the square root of the scattering intensity measured for the same individual AuNR. Using this correction, the quantum yields of all 82 single AuNRs were calculated as shown in Figure 6. Interestingly, the scatter in the PL intensities in Figure 4 is thereby strongly reduced for the quantum yields in Figure 6, presumably by reducing the effect of the spread in AuNR volumes. Further details of the calculation are provided in the Methods section.

According to the suggested mechanism in Figure 2B, the PL quantum yield in AuNRs is determined not only by the radiative decay probability from the emission state but also by the coupling strength between the absorption and emission states. In total, there are four rate constants involved in the PL process: k_1 and k_2 are the decay constants from the excited state (electron–hole pairs) to the ground state and the LSPR, respectively; k_3 and k_4 are the radiative and nonradiative decay constants for the LSPR mode, respectively. The overall PL quantum yield is $k_2/(k_1 + k_2) \times k_3/(k_3 + k_4)$. In molecules, higher excited states S_n usually first relax to the lowest excited state S_1, which then decays back to the ground state S_0 because $k_1 \ll k_2$. The fluorescence quantum yield is therefore simply given by the second factor, that is, the ratio of the radiative decay constant to the sum of all decay constants for S_1. In contrast, due to the high density of states, the dominating channel of the energy relaxation in the AuNRs is the nonradiative decay of the electron–hole pairs back to the ground state without exciting the LSPR ($k_1 \gg k_2$), and the quantum yield is therefore given by $(k_2/k_1) \times k_3/(k_3 + k_4)$. Assuming that the emission probability from the LSPR, $k_3/(k_3 + k_4)$, is proportional to the elastic scattering efficiency,[40] which is mostly independent of the AuNR aspect ratio (Figure 5C),[39] the overall PL quantum yield is mainly determined by k_2 as k_1 is determined by intrinsic properties of gold. Hence, we suggest that it is the decrease of the decay constant k_2 which is determined by the coupling strength between electron–hole pairs and the LSPR, causing the decrease of the PL quantum yield when the AuNR aspect ratio increases, as shown in Figure 6. In other words, with increasing energy gap between absorption and emission states, the electron–hole pairs are less likely to couple to the LSPR and to generate plasmon emission.

The PL quantum yield approximately displays an exponential decrease with increasing AuNR aspect ratio, as seen in Figure 6. It is interesting to again invoke a comparison to molecular systems. In molecules, k_2 is related to the transition probability rate constant, which can be obtained using Fermi's golden rule and yields the well-known energy gap law;[41] that is, the probability of nonradiative decay decreases exponentially with the energy gap. Our experimental data show a similar trend, which can be interpreted by a less efficient nonradiative coupling to the LSPR (k_2) as the energy gap increases. However, this is only a qualitative comparison because in molecules the nonradiative relaxation has to occur *via* multiphonon processes while intraband relaxation within the metal conduction band is dominated by fast electron–electron scattering and one-phonon assisted relaxation.

During the revision process of this work, a similar study of the PL quantum yield of AuNRs appeared by Orrit and co-workers.[42] Despite using a shorter excitation wavelength of 476 nm, their results are very similar to what we report here, including the magnitude of the quantum yield, considering that we estimated a slightly lower instrument detection efficiency. One of their main points is that the quantum yield increases by an order of magnitude for the transition from a spherical nanoparticle to a AuNR as interband relaxation is no longer an available decay mechanism for AuNRs. For AuNRs with LSPR peaks beyond 650 nm, they report no significant change in the quantum yield, in contrast to our results here. However, the decrease in quantum yield of a factor of ~5, which we observed here (Figure 6) for AuNRs with LSPR peaks between 600 and 800 nm, is not necessarily inconsistent with their spread in data that is displayed on a larger scale to highlight the difference to the nanospheres. While both of these studies provide important new insight into the one-photon luminescence of gold nanoparticles, more experiments are clearly needed to conclusively understand this interesting photophysical process in AuNRs and plasmonic nanoparticles in general.

CONCLUSIONS

In summary, our study has revealed new properties of the PL from an artificial molecule, especially the coupling between single excited electron−hole pairs and the collective behavior of free electrons. We have applied single-particle spectroscopy to study the PL quantum yield of AuNRs for which the energy gap between the absorption and emission states is variable by tuning the aspect ratio while keeping the excitation wavelength constant. The PL decreased exponentially with increasing energy gap for AuNRs with LSPR peaks between 600 and 800 nm. We assign this decrease to the change in coupling efficiency between excited electronic states and the surface plasmon (*i.e.*, the collective electron motion of the LSPR mode). Our results provide new insights into the mechanism of the PL from AuNRs and are important because of potential application in biosensing and imaging.[7,8] The PL could also be used to understand energy relaxation of hot electrons in metal nanoparticles, which is relevant for plasmon-enhanced photochemical reactions.[38]

METHODS

AuNRs were purchased from Nanopartz and characterized by transmission electron microscopy (TEM) using a JEOL 1230 and UV−vis extinction spectroscopy using a Ocean Optics S1024DWX spectrometer. The extinction spectrum of the AuNR solution is given in Figure S1A, which also shows a typical TEM image in the inset. The AuNR dimensions were determined from the TEM images and are summarized in Figure S1B. Afterward, they were spin-coated at low concentrations on quartz substrates. Scanning electron microscopy (SEM) for correlation with optical microscopy was carried out using a FEI Quanta ESEM2. Figure S2 shows the SEM image of the same area as in Figure 1.

The instrument setup is shown in Figure S3. A home-built instrument based on an inverted Zeiss microscope was used. Unless otherwise noted, excitation was carried out using the 532 nm line of a diode pumped continuous wave laser (Verdi V6, Coherent). A quarter-wave plate was inserted into the optical path to convert the laser light to circular polarization. The PL signal was collected by a 50× (NA = 0.8) air-spaced objective and passed through a dichroic filter, a notch filter (RNF-532, CVI), and a long-pass filter, which assured that all excitation light was removed from the signal. Alternatively, a 50/50 beam splitter was used instead of the dichroic filter because longer wavelengths were blocked by the dichroic filter. PL images were recorded using a scanning stage and an avalanche photodiode (APD, SPCM-AQR, Perkin-Elmer). Single AuNR spectra were collected by moving the sample to the location of a single AuNR and switching the detection to a spectrometer equipped with a CCD camera (Triax 190 and Symphony, Jobin Yovin). Because the collection efficiency depends on the polarization of the emission light, which in turn is dependent on the orientation of the randomly orientated AuNRs, a depolarizer was inserted before the spectrograph to minimize any polarization effects of the collection system. Typical excitation powers for the PL measurements were 200 μW at the sample with a spot size of 400 nm (fwhm). Transmission dark-field scattering spectroscopy was conducted on the same setup, with the notch and long-pass filters removed. The white light generated by a halogen lamp was focused on the sample by an oil-immersion condenser (NA = 1.4). The transmission dark-field setup measured plasmon scattering only without a contribution from plasmon absorption. For the PL measurements, the wavelength response of the collection system was corrected by a calibrated white light lamp (Figure S4).

The quantum yield Φ of the AuNRs was calculated from the measured PL spectrum according to eq 1:[43]

$$\Phi = \frac{N_{\mathrm{em}}}{N_{\mathrm{abs}}} = \frac{N_{\mathrm{signal}}}{\mathrm{Det.Eff}} \frac{h\nu_{532}}{\sigma_{\mathrm{abs}} I} \qquad (1)$$

N_{em} and N_{abs} are the number of emitted and absorbed photons per second, respectively. N_{signal} is the background-corrected signal intensity per second. I is the incident laser intensity, σ_{abs} is the absorption cross section at 532 nm with the energy of a 532 nm photon given by $h\nu_{532}$, and Det.Eff. is the detection efficiency, which was estimated to be 1%. The background-corrected signal was first corrected by the wavelength-dependent sensitivity curve given in Figure S4. The absorption cross section was calculated using COMSOL for different aspect ratio AuNRs (Figure 5). Using the polynomial fit and the dependence of the LSPR maximum on the aspect ratio (Figure 5B), each measured PL spectrum was corrected for the corresponding calculated absorption cross section. However, the absorption cross section was calculated for a constant AuNR width of 25 nm, while the experimental trend in Figure S1B shows that the width decreased with increasing aspect ratio. To correct for the effect of this volume difference on the absorption cross section, we have used the measured scattering intensity for each AuNR as an indicator for the actual AuNR volume, considering that the LSPR scattering intensity is proportional to the volume squared but insensitive to the aspect ratio (Figure 5C). We therefore divided the measured PL intensity by the square root of the dark-field scattering intensity for the same single AuNR, as absorption scales with the particle volume. To account for the fact that the scattering intensity was recorded in arbitrary units, we used the fact that the average width of the AuNRs with an aspect ratio from 2.5 to 2.9 was 25 nm, which is the same value as used in the calculation. Therefore the dark-field scattering intensity was first normalized in this range by calculating the average intensity for all AuNRs with an aspect ratio between 2.5 and 2.9 (LSPR maximum from 640 to 685 nm). The scattering intensity of all other AuNRs was then expressed as a relative intensity.

Conflict of Interest: The authors declare no competing financial interest.

Acknowledgment. This work was funded by the Robert A. Welch Foundation (C-1664), ONR (N00014-10-1-0989), NSF (CHE-0955286), and ACS-PRF (50191-DNI6). P.S. acknowledges support from the Royal Thai Government. We thank C. Landes, P. Nordlander, and N. Halas for useful discussions.

Supporting Information Available: Sample characterization; instrument setup; spectra corresponding to Figure 1; PL spectra with 488 nm excitation; excitation power dependence; DF scattering spectra taken before and after PL spectroscopy; effect of the numerical aperture on the PL and DF scattering spectra; effect of simultaneous laser excitation on the DF scattering spectrum. This material is available free of charge *via* the Internet at http://pubs.acs.org.

REFERENCES AND NOTES

1. Kulzer, F.; Orrit, M. Single-Molecule Optics. *Annu. Rev. Phys. Chem.* **2004**, *55*, 585–611.
2. Patterson, G.; Davidson, M.; Manley, S.; Lippincott-Schwartz, J. Superresolution Imaging Using Single-Molecule Localization. *Annu. Rev. Phys. Chem.* **2010**, *61*, 345–367.
3. Peterman, E. J. G.; Sosa, H.; Moerner, W. E. Single-Molecule Fluorescence Spectroscopy and Microscopy of Biomolecular Motors. *Annu. Rev. Phys. Chem.* **2004**, *55*, 79–96.
4. Timmerman, D.; Valenta, J.; Dohnalova, K.; de Boer, W. D. A. M.; Gregorkiewicz, T. Step-like Enhancement of Luminescence Quantum Yield of Silicon Nanocrystals. *Nat. Nanotechnol.* **2011**, *6*, 710–713.
5. Cherukuri, P.; Bachilo, S. M.; Litovsky, S. H.; Weisman, R. B. Near-Infrared Fluorescence Microscopy of Single-Walled Carbon Nanotubes in Phagocytic Cells. *J. Am. Chem. Soc.* **2004**, *126*, 15638–15639.
6. Durr, N. J.; Larson, T.; Smith, D. K.; Korgel, B. A.; Sokolov, K.; Ben-Yakar, A. Two-Photon Luminescence Imaging of Cancer Cells Using Molecularly Targeted Gold Nanorods. *Nano Lett.* **2007**, *7*, 941–945.
7. He, H.; Xie, C.; Ren, J. Nonbleaching Fluorescence of Gold Nanoparticles and Its Applications in Cancer Cell Imaging. *Anal. Chem.* **2008**, *80*, 5951–5957.
8. Wu, X.; Ming, T.; Wang, X.; Wang, P.; Wang, J.; Chen, J. High-Photoluminescence-Yield Gold Nanocubes: For Cell Imaging and Photothermal Therapy. *ACS Nano* **2010**, *4*, 113–120.
9. Wang, H.; Huff, T. B.; Zweifel, D. A.; He, W.; Low, P. S.; Wei, A.; Cheng, J.-X. *In Vitro* and *In Vivo* Two-Photon Luminescence Imaging of Single Gold Nanorods. *Proc. Natl. Acad. Sci. U.S.A.* **2005**, *102*, 15752–15756.
10. Mooradian, A. Photoluminescence of Metals. *Phys. Rev. Lett.* **1969**, *22*, 185–187.
11. Beversluis, M. R.; Bouhelier, A.; Novotny, L. Continuum Generation from Single Gold Nanostructures through Near-Field Mediated Intraband Transitions. *Phys. Rev. B* **2003**, *68*, 115433.
12. Varnavski, O. P.; Goodson, T.; Mohamed, M. B.; El-Sayed, M. A. Femtosecond Excitation Dynamics in Gold Nanospheres and Nanorods. *Phys. Rev. B* **2005**, *72*, 235405.
13. Mohamed, M. B.; Volkov, V.; Link, S.; El-Sayed, M. A. The 'Lightning' Gold Nanorods: Fluorescence Enhancement of over a Million Compared to the Gold Metal. *Chem. Phys. Lett.* **2000**, *317*, 517–523.
14. Imura, K.; Nagahara, T.; Okamoto, H. Plasmon Mode Imaging of Single Gold Nanorods. *J. Am. Chem. Soc.* **2004**, *126*, 12730–12731.
15. Farrer, R. A.; Butterfield, F. L.; Chen, V. W.; Fourkas, J. T. Highly Efficient Multiphoton-Absorption-Induced Luminescence from Gold Nanoparticles. *Nano Lett.* **2005**, *5*, 1139–1142.
16. Imura, K.; Nagahara, T.; Okamoto, H. Near-Field Two-Photon-Induced Photoluminescence from Single Gold Nanorods and Imaging of Plasmon Modes. *J. Phys. Chem. B* **2005**, *109*, 13214–13220.
17. Steiner, M.; Debus, C.; Failla, A. V.; Meixner, A. J. Plasmon-Enhanced Emission in Gold Nanoparticle Aggregates. *J. Phys. Chem. C* **2008**, *112*, 3103–3108.
18. Imura, K.; Okamoto, H. Properties of Photoluminescence from Single Gold Nanorods Induced by Near-Field Two-Photon Excitation. *J. Phys. Chem. C* **2009**, *113*, 11756–11759.
19. Wissert, M. D.; Ilin, K. S.; Siegel, M.; Lemmer, U.; Eisler, H.-J. Highly Localized Non-linear Optical White-Light Response at Nanorod Ends from Non-resonant Excitation. *Nanoscale* **2010**, *2*, 1018–1020.
20. Dulkeith, E.; Niedereichholz, T.; Klar, T. A.; Feldmann, J.; von Plessen, G.; Gittins, D. I.; Mayya, K. S.; Caruso, F. Plasmon Emission in Photoexcited Gold Nanoparticles. *Phys. Rev. B* **2004**, *70*, 205424.
21. Bouhelier, A.; Bachelot, R.; Lerondel, G.; Kostcheev, S.; Royer, P.; Wiederrecht, G. P. Surface Plasmon Characteristics of Tunable Photoluminescence in Single Gold Nanorods. *Phys. Rev. Lett.* **2005**, *95*, 267405.
22. Loumaigne, M.; Vasanthakumar, P.; Richard, A.; Debarre, A. Influence of Polarization and Wavelength on Two-Photon Excited Luminescence of Single Gold Nanospheres. *Phys. Chem. Chem. Phys.* **2011**, *13*, 11597–11605.
23. Tcherniak, A.; Dominguez-Medina, S.; Chang, W.-S.; Swanglap, P.; Slaughter, L. S.; Landes, C. F.; Link, S. One-Photon Plasmon Luminescence and Its Application to Correlation Spectroscopy as a Probe for Rotational and Translational Dynamics of Gold Nanorods. *J. Phys. Chem. C* **2011**, *115*, 15938–15949.
24. Wawilow, S. J. Die Fluoreszenzausbeute Von Farbstofflösungen Als Funktion Der Wellenlänge Des Anregenden Lichtes. II. *Z. Phys. A: Hadrons Nucl.* **1927**, *42*, 311–318.
25. Kasha, M. Characterization of Electronic Transitions in Complex Molecules. *Discuss. Faraday Soc.* **1950**, *9*, 14–19.
26. Munechika, K.; Chen, Y.; Tillack, A. F.; Kulkarni, A. P.; Jen-La Plante, I.; Munro, A. M.; Ginger, D. S. Quantum Dot/Plasmonic Nanoparticle Metachromophores with Quantum Yields That Vary with Excitation Wavelength. *Nano Lett.* **2011**, *11*, 2725–2730.
27. Gaiduk, A.; Yorulmaz, M.; Orrit, M. Correlated Absorption and Photoluminescence of Single Gold Nanoparticles. *ChemPhysChem* **2011**, *12*, 1536–1541.
28. Link, S.; Mohamed, M. B.; El-Sayed, M. A. Simulation of the Optical Absorption Spectra of Gold Nanorods as a Function of Their Aspect Ratio and the Effect of the Medium Dielectric Constant. *J. Phys. Chem. B* **1999**, *103*, 3073–3077.
29. Chang, W. S.; Ha, J. W.; Slaughter, L. S.; Link, S. Plasmonic Nanorod Absorbers as Orientation Sensors. *Proc. Natl. Acad. Sci. U.S.A.* **2010**, *107*, 2781–2786.
30. Tcherniak, A.; Ha, J. W.; Dominguez-Medina, S.; Slaughter, L. S.; Link, S. Probing a Century Old Prediction One Plasmonic Particle at a Time. *Nano Lett.* **2010**, *10*, 1398–1404.
31. Inagaki, T.; Kagami, K.; Arakawa, E. T. Photoacoustic Observation of Nonradiative Decay of Surface-Plasmons in Silver. *Phys. Rev. B* **1981**, *24*, 3644–3646.
32. Endriz, J. G.; Spicer, W. E. Surface-Plasmon-One-Electron Decay and Its Observation in Photoemission. *Phys. Rev. Lett.* **1970**, *24*, 64–68.
33. Lehmann, J.; Merschdorf, M.; Pfeiffer, W.; Thon, A.; Voll, S.; Gerber, G. Surface Plasmon Dynamics in Silver Nanoparticles Studied by Femtosecond Time-Resolved Photoemission. *Phys. Rev. Lett.* **2000**, *85*, 2921–2924.
34. Chu, M. W.; Myroshnychenko, V.; Chen, C. H.; Deng, J. P.; Mou, C. Y.; de Abajo, F. J. G. Probing Bright and Dark Surface-Plasmon Modes in Individual and Coupled Noble Metal Nanoparticles Using an Electron Beam. *Nano Lett.* **2009**, *9*, 399–404.
35. Varnavski, O. P.; Mohamed, M. B.; El-Sayed, M. A.; Goodson, T. Relative Enhancement of Ultrafast Emission in Gold Nanorods. *J. Phys. Chem. B* **2003**, *107*, 3101–3104.
36. Knight, M. W.; Fan, J.; Capasso, F.; Halas, N. J. Influence of Excitation and Collection Geometry on the Dark Field Spectra of Individual Plasmonic Nanostructures. *Opt. Express* **2010**, *18*, 2579–2587.
37. King, N. S.; Li, Y.; Ayala-Orozco, C.; Brannan, T.; Nordlander, P.; Halas, N. J. Angle- and Spectral-Dependent Light Scattering from Plasmonic Nanocups. *ACS Nano* **2011**, *5*, 7254–7262.
38. Novo, C.; Funston, A. M.; Mulvaney, P. Direct Observation of Chemical Reactions on Single Gold Nanocrystals Using Surface Plasmon Spectroscopy. *Nat. Nanotechnol.* **2008**, *3*, 598–602.
39. Jain, P. K.; Lee, K. S.; El-Sayed, I. H.; El-Sayed, M. A. Calculated Absorption and Scattering Properties of Gold Nanoparticles of Different Size, Shape, and Composition: Applications in Biological Imaging and Biomedicine. *J. Phys. Chem. B* **2006**, *110*, 7238–7248.

40. Sonnichsen, C.; Franzl, T.; Wilk, T.; von Plessen, G.; Feldmann, J.; Wilson, O.; Mulvaney, P. Drastic Reduction of Plasmon Damping in Gold Nanorods. *Phys. Rev. Lett.* **2002**, *88*, 077402.
41. Englman, R.; Jortner, J. The Energy Gap Law for Radiationless Transitions in Large Molecules. *Mol. Phys.* **1970**, *18*, 145–164.
42. Yorulmaz, M.; Khatua, S.; Zijlstra, P.; Gaiduk, A.; Orrit, M. Luminescence Quantum Yield of Single Gold Nanorods *Nano Lett.* **2012**, DOI: 10.1021/nl302196a.
43. Gaiduk, A.; Ruijgrok, P. V.; Yorulmaz, M.; Orrit, M. Making Gold Nanoparticles Fluorescent for Simultaneous Absorption and Fluorescence Detection on the Single Particle Level. *Phys. Chem. Chem. Phys.* **2011**, *13*, 149–153.